The ion-optical prototype of the low energy neutral atom sensor of the Interstellar Boundary Explorer Mission (IBEX)

M. Wieser[a] and P. Wurz
Physikalisches Institut, University of Bern, Sidlerstrasse 5, 3012 Bern, Switzerland

E. Moebius
Department of Physics and Institute for Study of Earth, Oceans and Space, University of New Hampshire, Durham, New Hampshire 03824, USA

S. A. Fuselier and E. Hertzberg
Lockheed Research Laboratories, 3251 Hannover St., Palo Alto, California 94304, USA

D. J. McComas
Southwest Research Institute, San Antonio, Texas 78238, USA

(Received 21 May 2007; accepted 10 November 2007; published online 26 December 2007)

The direct measurement of the energetic neutral atoms originating from the heliospheric termination shock and beyond as well as neutral interstellar gas penetrating into the heliosphere requires a very sensitive neutral particle imaging instrument in the energy range of 10–1000 eV. We present the development of the prototype of the low energy sensor for the Interstellar Boundary Explorer (IBEX) mission: IBEX-Lo is a neutral particle mass spectrometer dedicated to the measurement of energetic neutral atoms in this energy range. The response of the sensor to incident neutral hydrogen, helium, and oxygen atoms is discussed as well as the properties of the sensor's ion optics, the neutral-to-negative conversion surfaces, and other instrumental parameters. © *2007 American Institute of Physics.* [DOI: 10.1063/1.2821235]

I. INTRODUCTION

The solar system is moving relative to the surrounding local interstellar cloud (LIC) of warm and partially ionized interstellar gas (e.g. Ref. 1). The interstellar magnetic field and interstellar plasma are not able to enter the heliosphere, which is filled with the magnetized solar wind plasma. The heliosphere is sized and shaped by pressure balance between the LIC and the solar wind. At approximately 100 AU from the Sun, the solar wind is slowed down to a subsonic flow at the termination shock, which was recently encountered by Voyager 1.[2] Global models of the heliosphere-LIC interaction show that the two domains are separated by the heliopause, thought to be at approximately 140 AU, and perhaps a bow shock even further out in the ram direction.[3–5] Because of the relative motion of the Sun and the LIC, the neutral gas component penetrates deep into the inner heliosphere where the Sun's ultraviolet radiation together with charge exchange with the solar wind produces a cavity into the neutral gas flow within a few astronomical units around the Sun. This penetration of the interstellar neutral gas flow allows *in situ* diagnostics of the LIC material through pickup ions[6,7] and by direct neutral gas imaging,[8–13] done so far for interstellar helium by the Neutral Interstellar Gas Instrument (GAS) on the ULYSSES spacecraft.[11]

In the outer heliosphere the interaction of the solar and interstellar plasma components generates heated plasmas and energetic ions, which produce energetic neutral atoms (ENAs) via charge exchange with the penetrating interstellar neutral gas.[14] Because of the low densities the mean free path lengths for ENAs exceed the size of the heliosphere, and these particles can reach observers at 1 AU and can therefore be used like photons to generate images of the interaction in the outer heliosphere. Such ENA images will allow the determination of the strength and structure of the termination shock, provide information about acceleration processes at the termination shock, and determine properties of the solar wind flow beyond the termination shock and in the heliotail. Figure 1 shows a summary of presently available measurements of the energetic neutral atom inflow compared to results from different simulation models.[15] The simulations differ substantially, especially in the low energy region; thus more measurements in the energy range below 1 keV are required to better constrain the models and advance our theoretical understanding of the processes occurring at the termination shock.

In January 2005, NASA's Office of Space Science selected the Interstellar Boundary Explorer (IBEX) mission[16] for development and flight. IBEX will provide the first global views of the Sun's interstellar boundaries by taking angular resolved images of the global ENA flux at several energies in the range of ~10–6000 eV. IBEX will address the following key questions about the global interaction between the solar wind and the interstellar medium.

(1) What is the global strength and structure of the termination shock?
(2) How are energetic protons accelerated at the termination shock?

[a]Present address: Swedish Institute of Space Physics, P.O. Box 812, 98128 Kiruna, Sweden.

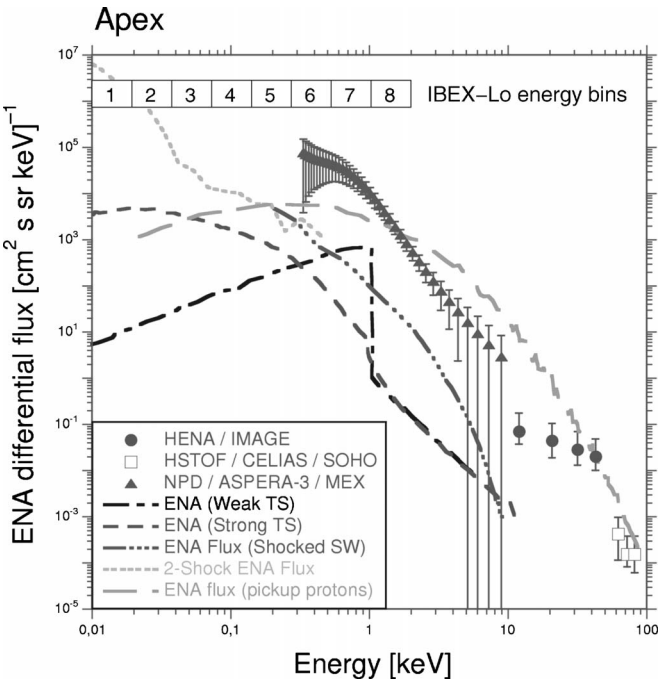

FIG. 1. Various calculated hydrogen ENA energy spectra together with available measurements (Ref. 15). The eight energy bins of IBEX-Lo superimposed on top fill the gap below 300 eV where no measurements are available.

(3) What are the global properties of the solar wind flow beyond the termination shock and in the heliotail?
(4) How does the interstellar flow interact with the heliosphere beyond the heliopause?

IBEX carries two ultrahigh sensitivity ENA single pixel cameras on a spinning spacecraft. Scheduled for June 2008, IBEX will be launched into a highly elliptical Earth orbit to get a view of the outer heliosphere beyond the Earth's relatively bright magnetospheric ENA emissions. The two sensors view perpendicular to the spacecraft-Sun direction. The spin axis of the spacecraft will remain roughly Sun pointed throughout the year, enabling both sensors to produce a nearly full sky map of the ENA flux every six months. The sensors cover different energy ranges with a substantial overlap: IBEX-Lo is sensitive for ~10–2000 eV and can separate neutral hydrogen and neutral oxygen atoms, whereas IBEX-Hi covers the range from 300 eV to 6 keV with very high sensitivity, but without mass resolution. IBEX-Lo's capability to detect neutral oxygen will also be used to observe the inflow of interstellar oxygen (science question 4 above). Both sensors are built out of similar functional modules: a collimator for setting the field of view and rejection of charged particles at the sensor entrance, followed by a conversion subsystem that transforms the incident ENAs into ions, a poloidal shaped electrostatic analyzer (ESA) for energy band selection, and a detector unit. Whereas in IBEX-Hi incident ENAs are positively ionized upon passage through a thin carbon foil, IBEX-Lo uses a charge conversion surface (CS) to convert the incident ENAs to negative ions (i.e., surface ionisation). To achieve high background and noise suppression, IBEX-Lo utilizes a triple coincidence time-of-flight (TOF) section, which also separates hydrogen and oxygen.[17] The TOF section is adapted from the flight-proven Cluster CODIF design.[18]

IBEX-Lo is not the first instrument to be used in space research to employ surface ionization to detect ENAs. The first instrument to use CS to ionize and characterize ENAs was the LENA instrument on the IMAGE mission, which used polycrystalline tungsten CS to record ENA images of the terrestrial magnetosphere and the auroral outflow region.[19,20] A recent review of ENA instruments is given in Ref. 21. The improvements in ENA instrumentation in this energy range have been dramatic since the realization of the LENA instrument. LENA had an angular resolution of $8° \times 8°$ (times 12 pixels), an entrance area of 1 cm^2, and a detection efficiency in the range from 10^{-5} to 10^{-3} (depending on energy).[20] IBEX-Lo has an angular resolution of $7° \times 7°$ (single pixel), an entrance area of 100 cm^2, and a detection efficiency in the range from 10^{-3} to 4.5×10^{-2} (depending on energy and species).

In this paper we describe the development of key components for the IBEX-Lo sensor and the related test results. We start with an overview of the design parameters, the related design choices, and a description of the individual subassemblies of the sensor prototype in Sec. II, followed by the test results for each of these subsystems in Sec. III. A discussion of the results and their consequences for the flight hardware design is laid out in Sec. IV, followed by the conclusions.

II. THE IBEX-LO PROTOTYPE

A. Overview

We have developed, built, and tested the prototype for the low energy sensor IBEX-Lo, a sensor for the detection, and separation of neutral hydrogen and oxygen atoms in the energy range of 10–2000 eV, which covers the typical energies of ENAs from thermalized solar wind and pickup ions at the termination shock. This energy range corresponds to velocity ranges of 10–150 km/s for O and about 30–600 km/s for H. These ranges cover the interstellar inflow velocities as seen from a spacecraft in Earth orbit.

Figure 2 shows a schematic drawing of the IBEX-Lo sensor. The sensor has a cylindrical symmetry. ENAs enter the sensor from the right through a collimator (CO) which sets the field of view and also suppresses charged particles from entering the sensor. The ENAs then hit the CS where a fraction of them is scattered as negative ions.[22] After moderate preacceleration (PreAC) and passing the poloidal ESA,[23,24] the negative ions are focused toward the center axis of symmetry. At the exit of the ESA the ions are postaccelerated to 20 keV prior to entering the TOF section where they are detected. The postacceleration (PostAC) helps to reduce the angular spread of the ion trajectories at the exit of the ESA. Without sufficient postacceleration, the angular divergence is increased compared to that at the entry of the ESA because the area of the exit aperture is smaller than the area of the entry aperture (i.e., the ion flux is concentrated during the passage through the ESA). As the energy of the particles remains constant during the passage

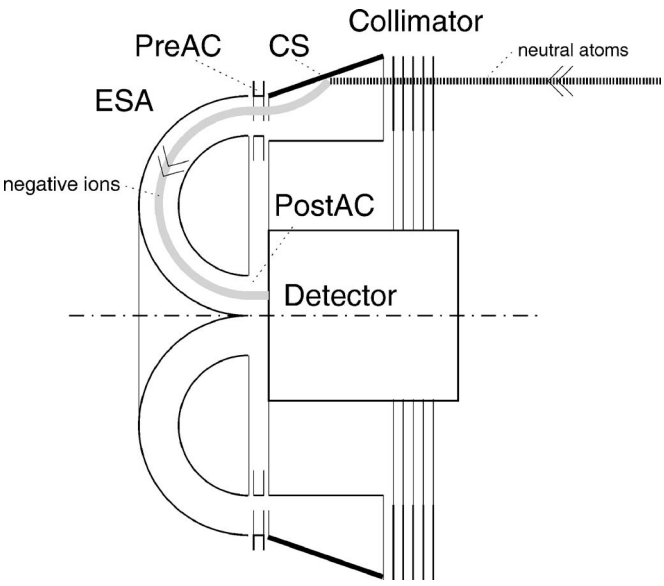

FIG. 2. IBEX-Lo prototype sensor concept. The sensor has a cylindrical symmetry. Neutral particles enter the sensor through a circular collimator, are converted to negative ions by reflecting from a conversion surface (CS), preaccelerated (PreAC), energyanalyzed and focused to the center by a poloidal energy analyzer (ESA), postaccelerated (PostAC), and finally registered in the detector section by an imaging microchannel plate (MCP) or a channel electron multiplier (CEM). For flight configuration the detector will be replaced by a time-of-flight section to get mass resolution.

through the ESA, an increase in the angular divergence is a consequence of phase space conservation (Liouville theorem). Substantial postacceleration is also needed for efficient detection and clear separation of oxygen in the TOF section which employs thin carbon foils to generate the start pulses for the consecutive TOF measurements.[17] Only particles above approximately 1 keV/nucleon pass these foils easily and without excessive energy and angular straggling. In the prototype, the TOF section has been replaced by a single imaging microchannel plate (MCP) detector system because detailed imaging of the ion trajectories was required for the development of the conversion surface and ion optics components. The TOF section, the collimator subsystem, and the combined conversion surface and ion optics subsystem have been evaluated and tested separately in order to address the specific design issues most effectively.

With the energy range of 10–2000 eV the sensor covers a range in the energy spectrum where only a few or no measurements are available to date (see Fig. 1). This energy range is subdivided into eight logarithmically spaced energy bins as shown in Table I, commensurate with the four key science questions.

The low neutral atom flux from the termination shock and beyond requires the sensor to have a large active area. Based on theoretical models[14] it was estimated that about 100 cm^2 are necessary for sufficient counts in each image pixel at each energy bin: depending on viewing direction, energy bin, and model assumption, count rates range from several per second down to 1 count/h. The total exposed conversion surface area of the sensor was fixed at 125 cm^2 corresponding to an outer radii of the conversion surface cone of 133 mm, which scaled the whole sensor. Figure 3 shows a cut-through drawing of the prototype sensor. For prototype testing only a part of the circumference was equipped with conversion surfaces to lower the complexity. The conversion surface section is shown on the left in Fig. 3.

TABLE I. IBEX-Lo energy bins.

Energy bin	Range (eV)
1	10–19
2	19–38
3	38–73
4	73–141
5	141–274
6	274–532
7	532–1030
8	1030–2000

B. Ion-optical design

The initial ion optics of the prototype were designed in only three weeks, using software for automatic ion-optics optimization developed at the University of Bern.[25] The main driver for the optimization was to maximize the overall transmission of the sensor, while keeping other constraints within defined limits: for example, energy resolution, angular divergence of the trajectories at the interface to the time-of-flight section, and variation of the collection efficiency of negative ions from different positions on the conversion surface. An additional complication was the angular scatter at the conversion surface that had to be matched by the angular acceptance of the ESA. We measured the angular scatter at the CS, which was used as input for the optimization, in a separated facility before.[25,26] Table II shows the performance of this design method in comparison to the earlier manual optimization of the ion-optical design (denoted "prior optimization" in Table II).

C. Hardware

1. The collimator

Neutral particles enter the IBEX-Lo sensor through the collimator section which limits the field of view to $7° \times 7°$ full width at half maximum (FWHM). The collimator is also designed to reject charged particles (electrons and ions), and it is common to both IBEX sensors. The only differences are that the mechanical dimensions are individually adapted to the sensor aperture and that the IBEX-Lo collimator contains a high-resolution quadrant with half the field-of-view angle for the observation of the interstellar oxygen flow.

The prototype collimator consists of a stack of 20 etched 100 μm thick stainless steel grid plates with a regular hexagon opening pattern. The grid plates are stacked on top of each other using spacers with predefined separations that start at values of approximately the linewidth of the hexagon boundaries and increase in a geometric progression [a schematic drawing is shown in Fig. 4(a)]. The collimator scheme is adapted from the implementation for the ACE SEPICA instrument.[27] The collimator design with its high ratio of hexagon diameter to linewidth of 5:1 (ratio $w:d$ in Fig. 4)

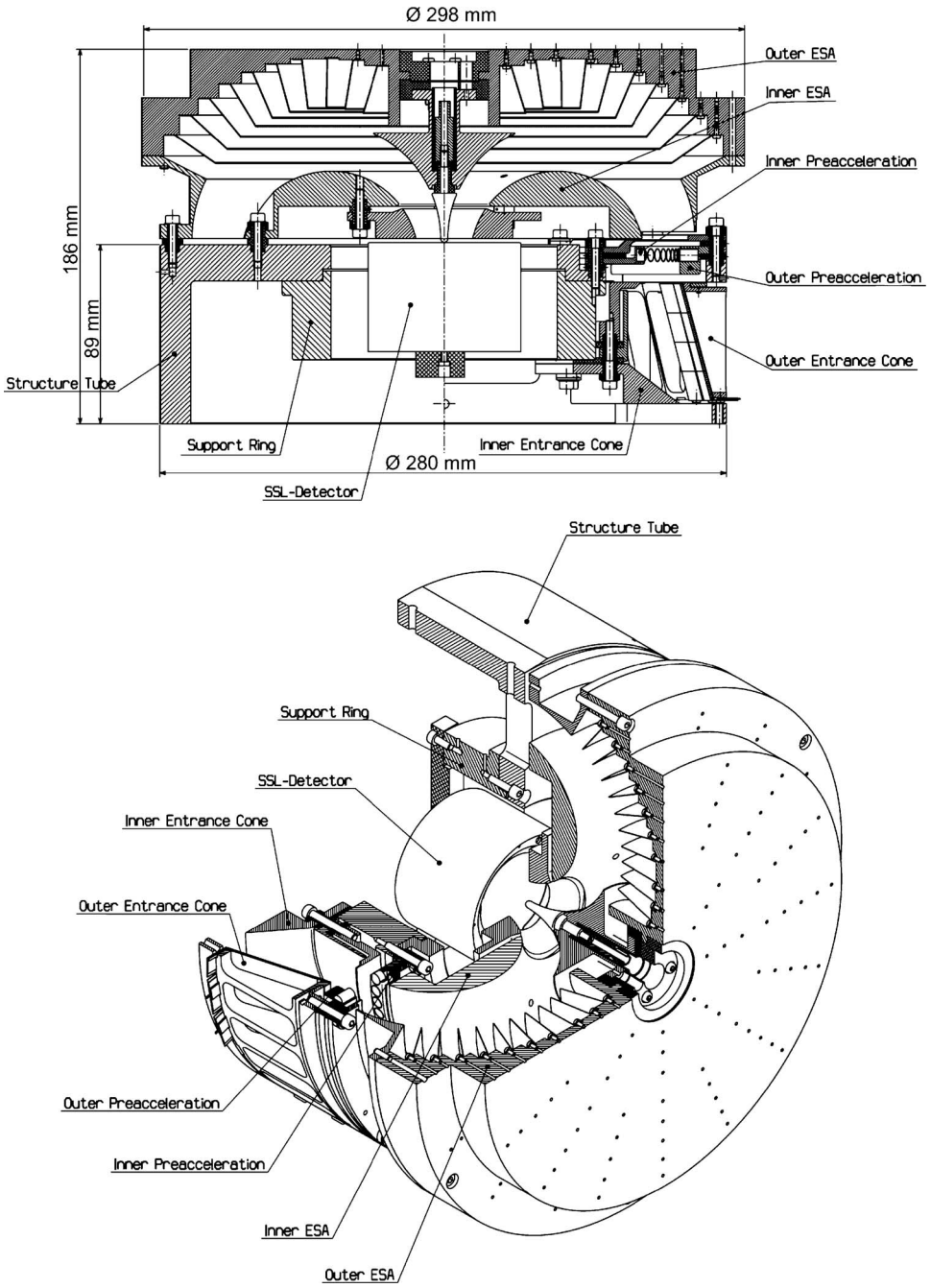

FIG. 3. Three-dimensional cut through the IBEX-Lo prototype. Only one quarter of the circumference is equipped with conversion surfaces to reduce complexity of the prototype. The collimator is not shown in this drawing. The size of the prototype as shown is 298 mm in diameter and 186 mm in length.

exhibits a high transmission of particles of >65%. The geometric progression of the grid separations suppresses leakage at large angles while minimizing the necessary weight and exposed surfaces for forward scattering of particles. Using a thin sheet material for the grids and achieving a sharp edge with etching minimize otherwise inevitable forward scattering of particles at material boundaries. For assembly the identically etched collimator grids were stacked on a jig with alignment pins that were positioned perpendicular to the baseplate with high precision. After the stacking, the colli-

TABLE II. Optimization constraints and drives for the automatic ion-optics optimization. "Prior optimization" refers to the manual optimization of the ion-optical system.

Simulation constraint	Objective	Prior optimization	After optimization
Transmission (conversion surface to exit of ESA)	>=0.5	0.07	0.5
Energy resolution $\Delta E/E$	<1	1.0	0.7
Angular divergence at exit of ESA (energy bin 4)	95% of trajectories <10° to normal	n/a	95% <7° to normal

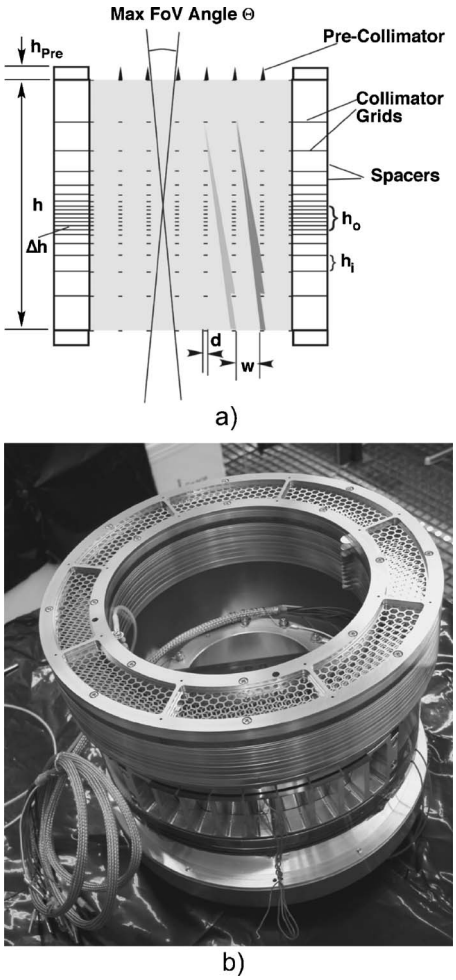

FIG. 4. (a) Schematic representation of the collimator. Etched plates with a thickness of $\Delta h = 100\ \mu m$ are stacked with spacers with a thickness of h_0 approximately equal the linewidth d in the center. The distance h_i increases geometrically toward both front and back sides. A precollimator on the front side improves further the suppression for large angles outside the field of view (FoV). (b) Complete IBEX-Lo prototype with collimator, which is about 300 mm in diameter.

mator plates were clamped with fasteners from both sides into the Ultem spacer, thus still providing the electrical insulation. Figure 4(b) shows the complete IBEX-Lo prototype including the collimator.

The front portion of the collimator assembly was insulated from the rear portion to allow for a positive repeller voltage of up to 10 kV in order to prevent positive ions from entering the collimator. To allow consecutive rejection of electrons and potentially generated secondary ions, provisions were made to implement two additional insulating spacers. For the future implementation of these additional insulating spacers with adequate material thickness, the geometric progression was rearranged while maintaining the performance. The design was simulated in a spreadsheet program to test for particle leakage outside the field of view by computing the angular coverage of each grid line as seen from the entry opening of a collimator channel.

The collimator was tested individually to characterize its angular acceptance and to identify potential leakage. The neutral beam from the calibration facility already provides

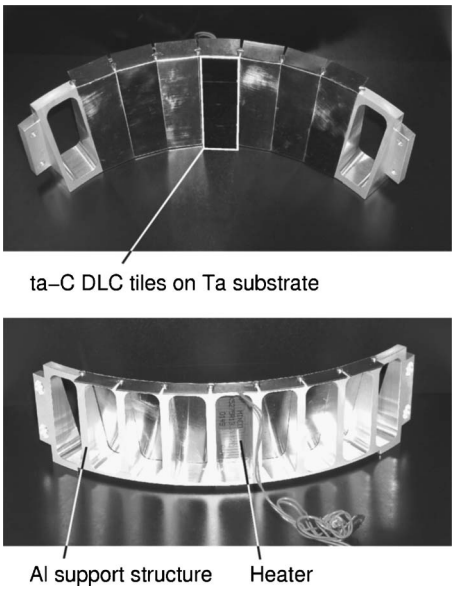

FIG. 5. Conversion surface support unit. The unit covers one quarter of the circumference of the prototype, divided into strips of about 20 mm width. For the prototype measurements only the center tantalum strip was equipped with four ta-C DLC tiles (top) because the testing was done with a neutral beam collimated down to this size. The total area equipped with ta-C tiles for prototype measurements was $20 \times 60\ mm^2$. A heater attached to the back side of the tantalum strip (bottom) allowed to study the effects of heating the surfaces up to 100 °C.

approximately the same angular divergence as set by the collimator.[28] Therefore, the collimator was not needed to test the characteriztics of the remainder of the prototype and a simple aperture was sufficient to mimic the collimator response. This made the characterization of the remaining system somewhat easier.

2. Conversion surface assembly

Several tetrahedral amorphous carbon (ta-C) diamondlike carbon (DLC) surface tiles polished to Ångström flatness were used as the conversion surface. The conical conversion surface area was covered with rectangular flat tiles with an average angle of incidence for neutral particles onto the conversion surface equal to 75° with respect to the surface normal. For test purposes only one 20 mm wide strip was furnished with conversion surface tiles, as the neutral beam provided by the neutral source was collimated down to a cross section of $15 \times 20\ mm^2$ prior entering the conversion surface assembly. Figure 5 shows the used conversion surface support structure. Conversion surface tiles were glued with spaceflight-approved glue onto tantalum strips with a heater attached to the back side. The CS can be heated to up 150 °C to remove adsorbates from the CS, which might impair its ionization capability. In the course of these investigations it was found out that the heaters are not necessary and the flight version of IBEX-Lo is not equipped with CS heaters.

3. Preacceleration and electron suppression

Prior to energy analysis, the negative ions leaving the conversion surface are preaccelerated away from the conversion surface into the ESA section to increase the ion collec-

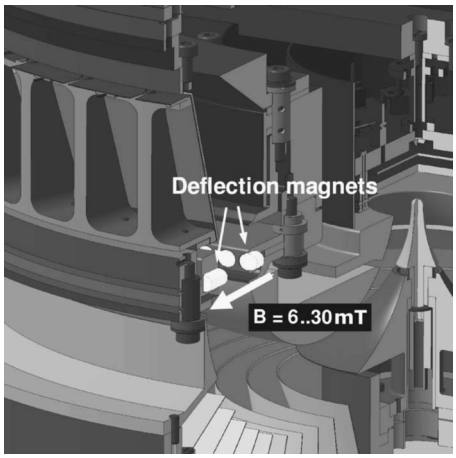

FIG. 6. Cut through the conversion surface assembly (top left), the electrostatic analyzer (bottom), and the imaging MCP in the center of the sensor (top right). The secondary electron suppression magnets embedded in the inner and outer preaccelerator electrodes are shown in white.

tion efficiency from the conversion surface. Depending on the location on the conversion surface, the collection efficiency is between 100% (closest to ESA) and 60% (end furthest away from ESA).

Secondary electrons generated at the conversion surface by particle impact or energetic photons are suppressed from entering the ESA by magnets placed in the preaccelerator electrodes. Suppression is needed as diamondlike conversion surfaces are efficient secondary electron emitters[29] and the photoelectron yield for UV photons is in the range of $10^{-3}-10^{-2}$. Without magnets, severe contamination of the ion signal by secondary electrons would happen during observations in space. Of course, the TOF system easily discriminates ions against electrons. However, the TOF system is very efficient with a very low background countrate to handle signals at the level of counts/down to counts/h and even lower.[17] The drawback of such a TOF system is that the electronics will saturate from the electrons, even though the TOF could discriminate these according to time of flight. Also, an increased TOF background will result from a large flux of electrons (or photons) into the TOF system via a process known as false coincidences. Even using the IBEX-Lo prototype the electrons are noticeable in the two lowest energy bins without the magnet system. The magnets deflect the electrons originating from the conversion surface and surrounding electrodes in tangential direction away from the direct path to the ESA exit by a radial magnetic field with a strength between 6 and 30 mT (Fig. 6). The magnets were placed at the location of the narrowest gap in the ion path, between ESA and conversion surface assemblies, to be most effective with moderate magnetic field strengths, without disturbing the ions even at low energies. Two different schemes for mounting the magnets were evaluated: face-on mounting without blackening of the front surfaces [Fig. 7(a)]; mounting behind a blackened surface (Cu_2S, Scheering Rapid[30]) with serrations [Fig. 7(b)].

Both methods performed equally well for the suppression of electrons. The latter method was finally chosen for better suppression of neutral particles hitting these electrodes.

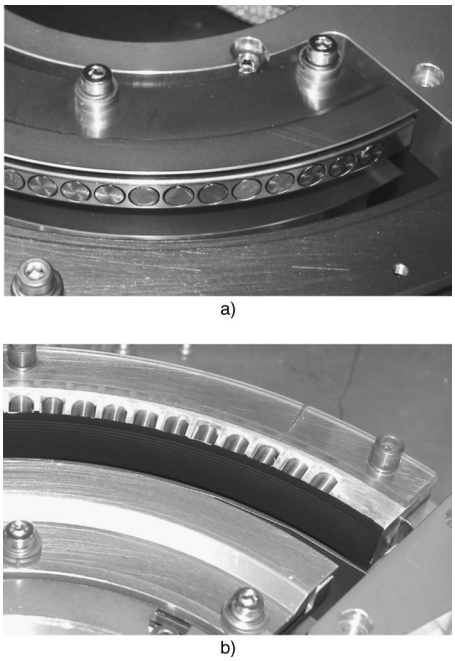

FIG. 7. (a) Secondary electron suppression magnets embedded in the preaccelerator electrodes (inner electrode is shown, view from the ESA side). For this configuration the electrode surface is coated with iridite and the magnets themselves are untreated AlNiCo. The outer electrode looks the same in this configuration. Individual magnet rods are 6 mm in diameter. (b) Configuration with magnets hidden behind a blackened and serrated electrode surface (outer preaccelerator electrode is shown, view from the ESA side). The inner electrode surface (not visible) also has serrations in this configuration.

Microserrations have been applied to the inner and outer preacceleration electrodes (see Fig. 3), and the outer ESA electrode was built as finned structure (see below). Furthermore, all electrodes enclosing the ion trajectories were blackened in the end. Figure 8 shows an electron microscope image of copper sulfide blackened microserrations with a pitch of 140 μm similar to those used on the prototype sensor. Particles hit the serrations from the right. The rough Cu_2S surface absorbs the impacting particles with high efficiency, thus effectively eliminating particles on non-nominal trajectories. Cu_2S-blackened surfaces also absorb UV radiation very well.[31] Combined, these measures result in a much improved overall signal-to-noise ratio.

4. Electrostatic analyzer

Energy analysis of the converted ions from the conversion surface is done in the poloidal energy analyzer (ESA). The energy resolution of the ESA in the prototype is about $\Delta E/E \sim 0.7$. This relatively moderate resolution was chosen to increase the transmission of the ESA, to reduce the duty cycle when sweeping through all energy bands, and to match the width of the energy bands (given in Table I). The ESA also bends the particle trajectories by 180° as is required for suppression of photons and neutral particles not converted at the conversion surface. The wide gap between the inner and outer ESA electrodes, because of the large $\Delta E/E$, makes suppression of scattered particles a severe challenge. Several absorption schemes were investigated for the ESA electrodes to get best suppression of neutral particles and photons origi-

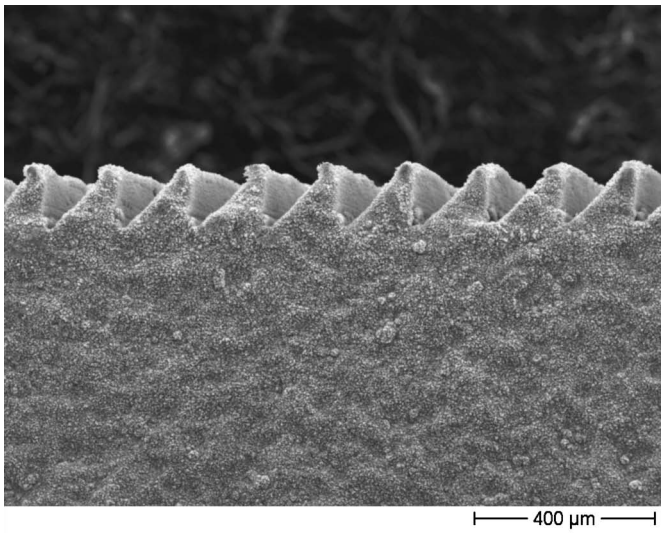

FIG. 8. Electron microscope images of copper sulfide-blackened microserration structure, Image by E. Krähenbühl, Institute of Applied Physics, University of Bern.

nating from the conversion surface or neutral particles created from ions hitting the ESA electrodes: flat electrodes with Iridite coating: blackened surfaces (Cu_2S, Scheering Rapid[30]) with microserrations (Fig. 8); blackened surfaces with fins in the outer ESA electrode (Figs. 3 and 9).

The fins shown in Fig. 9 are oriented such that a particle originating from the entry side of the sensor and hitting the fins does not have a direct line of sight from the impact location on the electrode to the exit of the ESA. The fin assembly replaces the previously used outer ESA electrode. For ease of operation, the fin assembly was set on ground potential all the time. In order not to change the field configuration compared to the flat and serrated outer ESA plate, the fin tips were moved outwards, resulting in a larger ESA gap while keeping the electric field in the ESA gap the same. Careful ion-optical simulations verified that the energy resolution was not affected by this change; higher energy ions

FIG. 9. Outer ESA electrode with fins. Particles from the conversion surface always hit the fins on a face with no direct line of sight from the impact point to the ESA exit. The complete assembly is 298 mm in diameter.

outside the ESA passband were now absorbed on the remaining cone of the outer ESA plate closer to the center axis of the sensor (see Fig. 3). All fins were individually electroformed, Cu_2S blackened, and then mounted onto an aluminum back plate.

5. Postacceleration and detection

At the exit of the ESA, the particles are postaccelerated to a potential up to 20 kV prior to entering the TOF unit. For practical reasons during the tests, the imaging detector was placed closer to the ESA exit, allowing us to lower the detector potential to 2275 V for an MCP detector and 10 kV for a channel electron multiplier (CEM) detector, respectively, while maintaining the field configuration and field strength at the ESA exit. Nevertheless it limited the maximum bin number that was accessible for each detector: the imaging MCP detector could be used for bin 1 with 14 eV center energy to bin 5 with 197 eV center energy, whereas the nonimaging CEM detector could make measurements up to bin 7 with 741 eV center energy (Table I).

III. SENSOR CHARACTERISTICS

A. Test environment

Tests with the IBEX-Lo prototype were performed in the CASYMS (Ref. 32) calibration facility for ion tests and in the MEFISTO (Ref. 33) calibration facility for neutral beam measurements. Both facilities are located at the University of Bern.

The angular acceptance of the ESA was matched to the angular scatter the particles suffer by scattering from the CS. Thus, particles travelling inside the angular acceptance of the ESA should all be transmitted, and particles scattered outside the angular acceptance of the ESA have to be effectively suppressed, by the serrations, the fins, and the blackening. The measurement of this suppression was performed by replacing the conversion surface with a pinhole. A collimated ion beam was directed through this pinhole at various angles of incidence to the surface normal from the outside (Fig. 10) to cover more than the full two-dimensional angular extend of the scattered particles. The two-dimensional images obtained from the imaging MCP detector[34] together with the

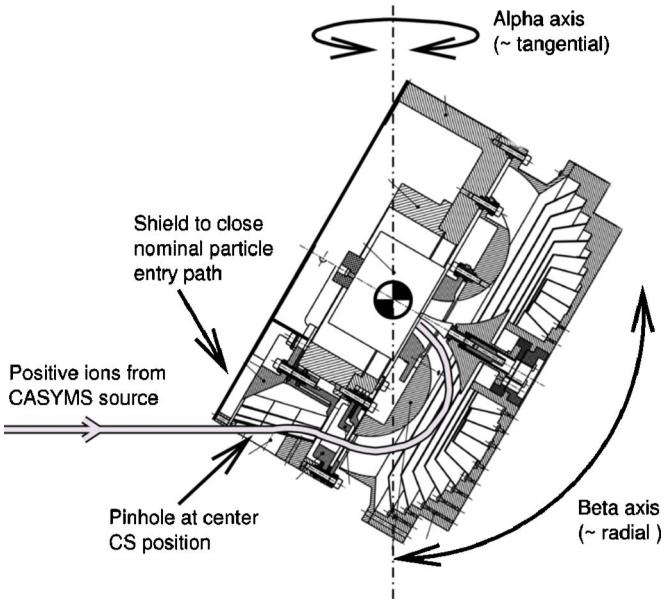

FIG. 10. Setup for ion tests. The ion beam enters the prototype through a hole in the conversion surface plane. Different reflection angles of incident neutral particles are simulated by rotating the prototype relative to the incoming ion beam.

ion-optical simulations made it easy to distinguish between nominally transmitted particles forming a sharp image of the pinhole in the conversion surface at the detector plane, and scattered particles that appear more randomly distributed in the image. The two parts were then separated in the image to estimate the total amount of scattering for this specific angle of the ion beam relative to the conversion surface plane. By integrating over all angles the total scattering in the sensor was calculated.

All other properties of the sensor were investigated using neutral particles impinging on the ta-C DLC conversion surface. A schematic representation of the setup is shown in Fig. 11. Neutral particles were produced by reflecting a monoenergetic positive ion beam at grazing incidence from a tungsten surface.[28] After removing the remaining charged particles via electrostatic deflection, a neutral beam with an energy width FWHM of about 15% of the incident ion energy and a mean energy of about 85% of the incident energy exits from the beam neutralizer device. The neutral atoms then reach the conversion surface of the prototype after passing a collimator plate, limiting the divergence of the neutral beam to $4° \times 10°$, a value comparable with what the omitted collimator would provide. Figure 12 shows the prototype installed in the MEFISTO calibration facility.

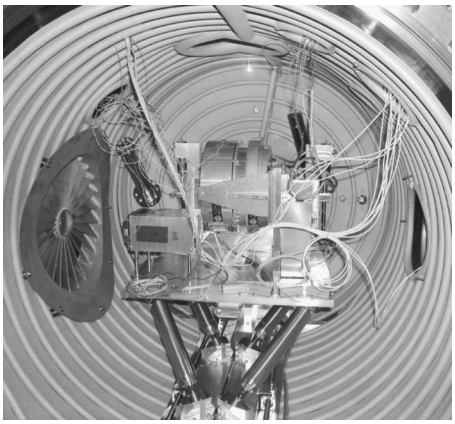

FIG. 12. IBEX-Lo prototype (cylindrical structure in the center) installed in the MEFISTO calibration facility of the University of Bern, Switzerland. The ion beam enters the chamber from the left through the fan-shaped opening. The ion beam is neutralized in the box left of the center of the image (Ref. 28) prior to entering the IBEX-Lo prototype. Most electrostatic shielding around the prototype setup was removed for this picture.

The collimator performance was evaluated separately from the rest of the prototype. The angular response and the ion suppression of the collimator were determined using an imaging MCP detector placed directly behind the collimator stack. The entire assembly was then tilted in two dimensions relative to the incident ion beam to get the full angular response. Charged particle rejection was tested by applying high voltage to the front grid plates and spacer of the collimator. The collimator assembly was tested in the CASYMS facility, and Fig. 13 shows the used test setup.

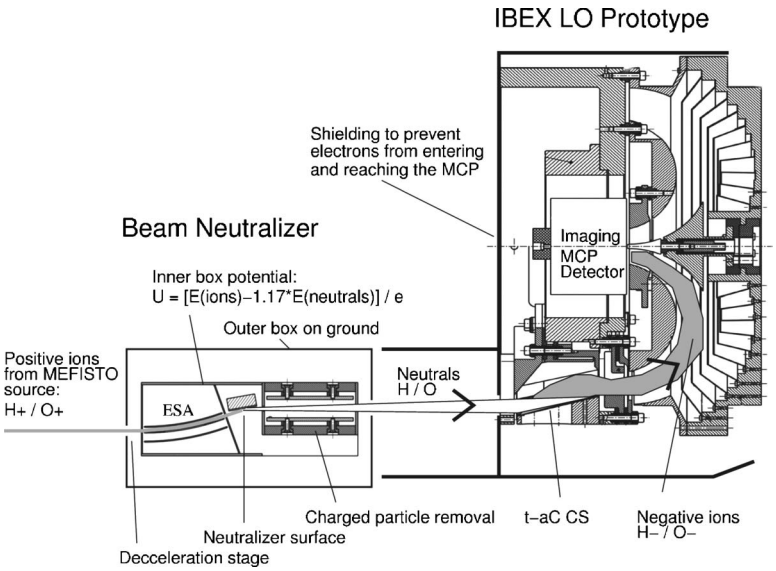

FIG. 11. Setup used for neutral particle tests. The prototype is mounted at a fixed position relative to the ion beam neutralizer (Ref. 28) which provides a neutral beam with similar angular characteristics as the separately evaluated collimator. The neutral beam energy is adjusted by changing the potential U of the inner box of the neutralizer containing the neutralizer surface, while the energy of the incident positive ions is kept constant. The factor of 1.17 in the formula for the floating potential accommodates for the energy loss at the neutralizer surface.

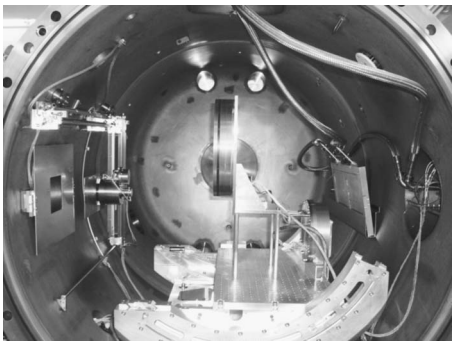

FIG. 13. IBEX-Lo prototype collimator (cylindrical structure in the center) installed in the CASYMS calibration facility of the University of Bern, Switzerland. The ion beam enters the chamber from the left through the rectangular opening. The imaging MCP detector is mounted behind the bottom section of the collimator.

B. Angular resolution

Using the multiple axis scanning capability of the mounting in the CASYMS facility the angular response, edge scattering, and the leakage outside the nominal field of view were characterized for the IBEX-Lo prototype collimator. Figure 14 shows the relative transmission (normalized to the maximum count rate) of the collimator in gray shading as a function of the two tilt angles in the CYSMYS facility (alpha and beta) from −7° to +20° in both angles. The inset shows the orientation of the hexagon pattern along with two adjacent cuts separated by 60° perpendicular to the grid lines. The main transmission is concentrated around the nominal pointing direction, as it should be. The measured angular acceptance is 7° FWHM. Also visible are two distinct areas with patterns outside the field of view, indicating a small leakage with transmissions of up to a few percent. The maxima of these patterns are aligned with the cuts perpendicular to the grid lines, where it is, in fact, most challenging to close a collimator with a large open-width to line-width ratio. The leakage outside the field of view is also seen in this cut between 12° and 30° angle off center. The exact leakage pattern was identified in simulations when all trajectories passing each individual grid edge were included. They had been overlooked in the original simulations, which only concentrated on trajectories from the edges of the entry and exit plates. The leakage has been completely eliminated with improved spacer sequencing in the flight hardware design based on the updated simulations. This was independently verified in Monte Carlo simulations. The range between 10° and 12° off the center peak provides an upper limit for the scattering of particles at the grid edges of $<10^{-4}$. Only an upper bound can be given due to the limited dynamic range of the imaging detector used, since this measurement is limited by the dark count rate of the imaging detector.

C. Verification of ion-optical optimization

The correctness of ion-optical optimization software was successfully validated by comparing the simulations with measurements. An example of such a validation is shown in Fig. 15: measured and simulated intensity profiles at the ESA-TOF interface are shown. A low divergence neutral oxygen beam of 64 eV center energy was used to illuminate

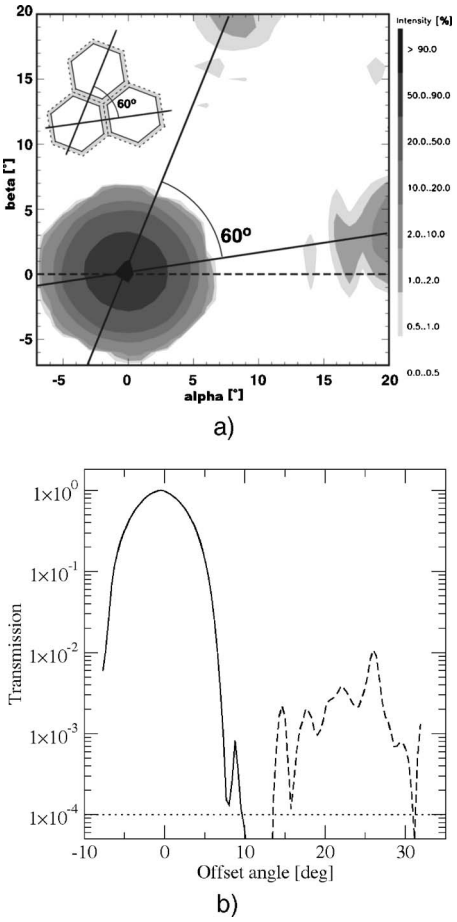

FIG. 14. (a) Relative transmission (normalized to the maximum count rate) of the prototype collimator in a two-dimensional angular scan. The inset shows the orientation of the hexagon pattern relative to the scan directions. The full lines, separated by 60°, in the scan and the inset mark cuts through the pattern perpendicular to the grid lines. Nominal performance is obtained except in the direction of the solid lines, where some leakage is visible (see text). (b) shows a profile of the transmission along the dashed line in (a). The angular width of the center peak (solid line) is just under 7° FWHM. The observed leakage is shown as a dashed line. The dotted line indicates the limit of the dynamic range of the detector used.

the conversion surface in both cases. A geometry as shown in Fig. 11 was used—resulting in the characteristic semicircle-shaped beam profile at the exit of the ESA. Good agreement between measured and simulated data is found. The larger scattering in the simulated data is due to an overestimation of the angular scattering at the conversion surface in the simulation.

The simulated and the measured energy resolution are compared in Fig. 16. Again, there is good agreement between simulated and measured data, proving the correctness of the ion-optical design.

D. Energy resolution

Energy bins of the sensor were evaluated by varying the incident neutral atom energy, while the sensor was set to a fixed energy bin (Fig. 16). The sensor design was optimized for 20 kV postacceleration. Due to limitations in the maximum float voltage of the imaging detector of 2250 V, the detector was moved closer to the exit of the ESA, effectively reducing the postacceleration voltage needed while maintain-

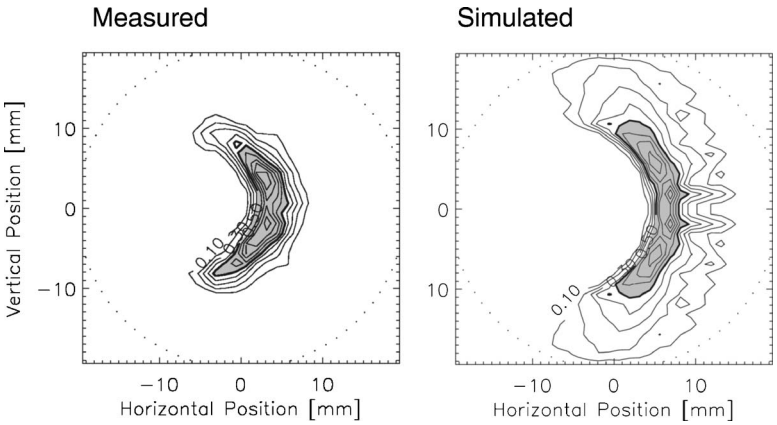

FIG. 15. Measured beam cross section at the exit of the annular ESA when the conversion surface is illuminated with a low divergence neutral oxygen beam with 64 eV average particle energy (left). The 50% intensity level is shown in gray. The larger scatter in the simulated image (right) is due to an overestimation of the angular scattering at the conversion surface in the simulation.

ing the electric field strength in the postacceleration gap at the exit of the ESA. The resulting distortions in the energy bin shape are negligible for the lower energy bins with center energies for the incident neutrals of less than 102 eV (bin 4) as verified by ion-optical simulations. An energy resolution of the prototype of $\Delta E/E=0.98$ was measured for bin 4. After correction for the energy spread of the incoming neutral atoms, this gives an energy resolution of 0.7 in good agreement with the ion-optical simulation. For bin 5 with 197 eV center energy, the distortions in the shape of the transmission curve become noticeable as the potential of the postacceleration electrodes approaches the 2250 V front face potential of the imaging detector. Energy bins with higher center energy were evaluated by replacing the imaging detector by a nonimaging CEM that allowed the detector float voltage up to 10 kV and made the upper energy bins accessible for evaluation (see Fig. 16). Only the highest bin, centered at an energy of 1500 eV, could not be tested with these detectors. However, given the good agreement of the ion-optical simulation with the performance of the prototype for every parameter we can compare, we are very confident that the instrument will have the predicted performance also for the one energy bin that was not accessible to measurements with the prototype instrument.

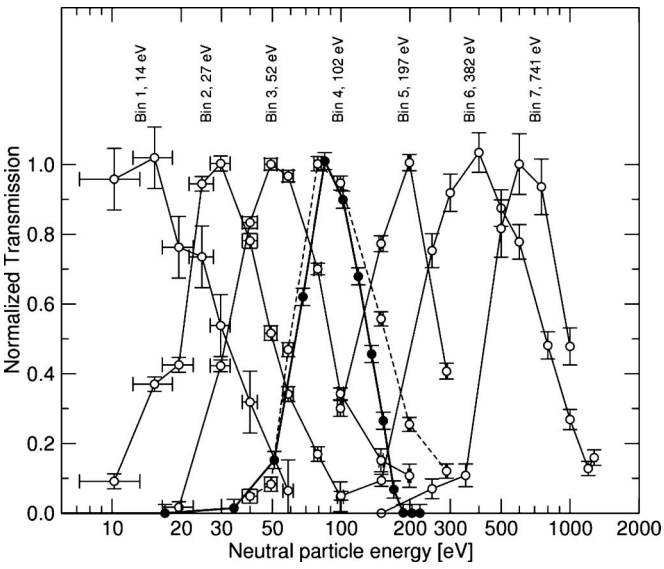

FIG. 16. Seven out of eight energy bins of the prototype (open circles) measured with two different detectors. Bins 1–5 were measured using an imaging MCP set to 2250 V float potential and bins 6 and 7 with a CEM set to 10 kV float potential. Bins 5 and 7 show some distortion as the center energy approached the maximum energy possible for the detector float voltage used. Nevertheless the energy bins remain well defined. The expected theoretical response for a monoenergetic neutral beam is shown for bin 4 (solid circles, bold line). The deviation from the measurement (dashed line) on the high energy side of the peak is due to the energy distribution created in the beam neutralizer.

E. Conversion efficiency and geometric factor

The neutral-to-negative ion conversion efficiency of the ta-C DLC surfaces is in the range of 0.5%–5% for hydrogen in the energy range of interest. Data obtained from the prototype measurements fit well to values measured earlier with different setups and experiments [Fig. 17(a)]. The geometric factor of the sensor was obtained by absolute calibration of the detection efficiency at the center of each energy bin. Data for the five lowest energy bins with center energies up to 197 eV are available. Above 52 eV center energy the efficiency needs to be corrected for the low postacceleration of 2250 V instead of 20 kV, based on our detailed ion-optical calculations. Figure 18 shows the geometric factor of the prototype for incident neutral hydrogen. The energy dependence of the geometric factor mostly arises from the energy dependent ionization efficiency and to a lesser extent from the energy dependent scattering properties of the conversion surface. For neutral energies below 50 eV the geometric factor could be measured directly. Between 50 and 200 eV the values were corrected for the lower than nominal postacceleration voltage used due to limitations in the operating mode of the imaging detector. Above 200 eV the geometric factor was extrapolated based on the ionization efficiency of the conversion surface (Fig. 17) and on detailed ion-optical simulations for the nominal postacceleration voltage of 20 kV.

F. Suppression of scattered particles

Given the low count rates expected for the IBEX mission and the large ESA gap width, the efficient suppression of particles scattered inside the ion optics is crucial. Given that the ionization rate goes from 10^{-3} to a few 10^{-1}, depending on species and energy (see Fig. 17), most of the incoming neutral atoms leave to conversion surface as neutral atoms and enter the ESA. If we ask for a signal-to-noise ratio of at least 10 at the lowest energy bin, we need a suppression

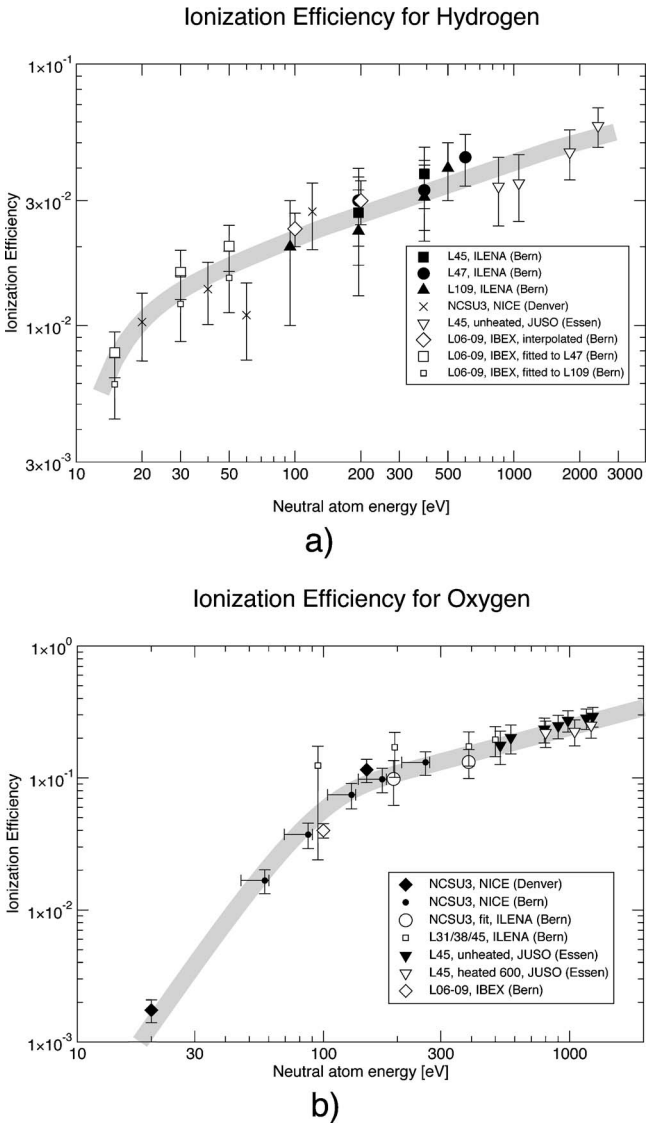

FIG. 17. Ionization efficiency for hydrogen (a) and oxygen (b) off various ta-C DLC conversion surfaces as used in the prototype measured in different experiments in Bern (IBEX, ILENA), Essen (JUSO), and Denver (NICE). The data set labeled NICE was taken from (Ref. 35).

scattered particles of 10^4 in ESA. Note that the TOF unit, which will be used in the flight version, cannot distinguish between scattered and nominal particles since it does not have an imaging capability.

Three different configurations were investigated (Table III). For all three configurations the fraction of directly transmitted particles remained constant within the measurement uncertainties. The fraction of particles scattered at electrodes toward the detector at the exit of the ESA was reduced by a factor of about 10 by introducing blackened serrations and by a factor of >190 by introducing blackened fins in the outer ESA electrode. The measurement uncertainties for the detected scattered fraction are about 20% of the value shown for the first two configurations. In the configuration with blackened surfaces and fins only an upper limit of the scattered particle fraction can be given due to counting statistics. However, this upper limit meets the requirement for suppression mentioned above. In addition, ion generated at the CS but being outside the selected energy band of the ESA have

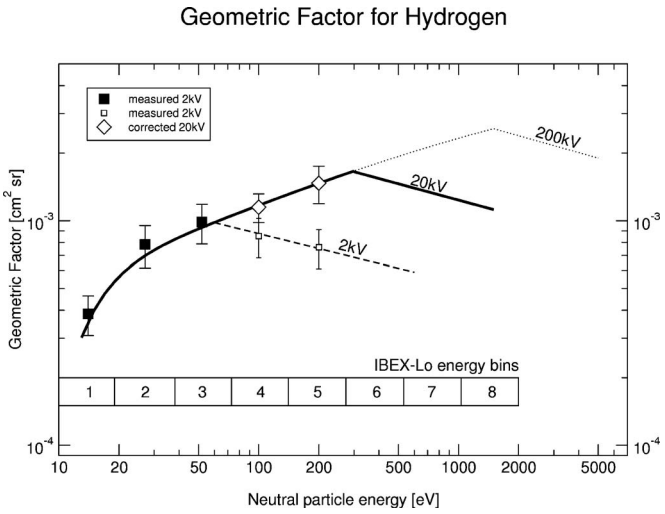

FIG. 18. Geometric factor of the prototype for different postacceleration voltages. At low energies the geometric factor is governed by the ionization efficiency at the conversion surface (closed black squares). At higher energies the geometric factor depends on the postacceleration (small open squares, for 2 kV postacceleration). A postacceleration of 20 kV will increase the geometric factor (open diamonds) for higher energies. The solid line shows the expected geometric factor over the whole energy range (fit at lower energies, simulation at higher energies) for 20 kV postacceleration. For even higher postacceleration the geometric factor would increase further (dotted line).

to be absorbed by the structure without causing a significant background signal. Furthermore, blackened surfaces, blackened serrations, and blackened fins are also an optimal solution for suppression of UV photons entering through the collimator.

G. Suppression of secondary electrons

In flight, a large source of secondary electrons originating from the conversion surface is due to photoelectrons. The Lyman-α flux from the dark sky is about 800 R (and much higher if a star is in the field of view), which corresponds to a photon flux of about 6.8×10^7 cm^{-2} sr^{-1} s^{-1}. For the IBEX-Lo sensor with its large aperture this results in about 10^7 s^{-1} Lyman-α photons entering the sensor, and a photoelectron flux of up to 10^5 s^{-1} released from the CS, since the diamondlike surface is also a good photocathode. These electrons will propagate through the ESA until the TOF unit (mostly for the lowest energy and second lowest bins), unless they are removed on their way. In principle, the TOF system could easily discriminate ions against electrons based on the large difference in mass. However, the TOF system is very efficient and with a very low background countrate to handle signals at the level of counts/s down to counts/h and even lower. The drawback of such a low-signal and low-background system is that the TOF electronics (the start event counter) will saturate from the electrons and paralyze the TOF measurement. Even if the TOF would be able to handle the flux of electrons and discriminate them according to time of flight, the remaining the problem are the accidental coincidences causing a contribution to the background signal. Thus, we concluded that the secondary electrons have to be hindered from reaching the TOF unit. The measures taken

TABLE III. Suppression of scattered particles.

Prototype configuration	Fraction of directly transmitted particles	Fraction of detected scattered particles
No blackening, no serrations or fins	0.50±0.02	3.24×10^{-2} (uncertainity see text)
Blackened surfaces, with serrations	0.47±0.02	3.04×10^{-3}
Blackened surfaces, with fins	0.48±0.02	$<1.70\times10^{-4}$

for the electron suppression also help to suppress the propagation of UV photons to the TOF unit, which which causes the same problems.

The effectiveness of the secondary electron suppression was evaluated using different prototype configurations. Secondary electron suppression with permanent magnets proved to be very effective in removing the unwanted electrons while not affecting the negative ions noticeably. The magnets used produce a radial field of 6–30 mT in the gap between the inner and outer preacceleration electrodes. See Fig. 3 for the location of these electrodes and Figs. 5–7 for the details of the magnet accommodation. Figure 19 shows a comparison between measurements with and without secondary electron suppression magnets for the most affected energy bin 1 with 14 eV center energy. A neutral hydrogen beam was used for these measurements. The prototype energy bin setting was kept constant while sweeping the incident neutral atom energy. The imaging detector measured total counts independent of particle species in this configuration always at a final ion energy of 2250 eV. With magnets, a substantial reduction in the count rate at the detector is obtained. Above an energy of 70 eV of the primary neutral atoms the count rate increases again because of the strong increase of sputtered negative ions from the conversion surface. These contributions to the signal are identified in Fig. 19. In the flight sensor the sputtered particles will be separated from the true signal by making use of the time-of-flight data from all energy bins. For energy bin 2, with 27 eV center energy, also a smaller signal was observed when using the magnets, but to a lower extent because the energy distribution of the secondary electrons and the energy distribution of sputtered particles both peak at a few eV. For the higher energy bins no effect was observed because the center energy of these bins is too far away from the secondary electron energy distribution and sputter energy distribution.

The different mounting schemes for the magnets in the electrodes (face on and hidden behind blackened serrations) performed equally well in terms of secondary electron suppression. However, particle scattering was minimized by the version with serrations.

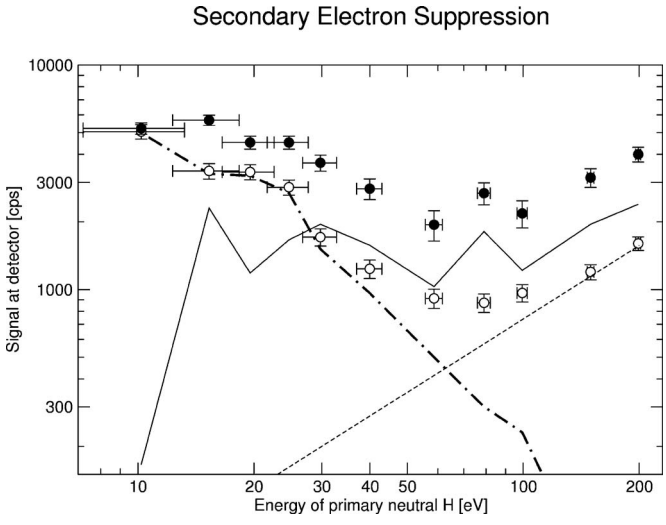

FIG. 19. Transmission of prototype for energy bin 1 with 14 eV center energy is shown with data from a sensor with (open circles) and without (closed circles) secondary electron suppression magnets. The difference between the two sets corresponds to the secondary electrons generated at the conversion surface (solid line). The contribution of sputtered particles was estimated (dashed line) and subtracted from the data obtained from a sensor with suppression magnets resulting in the fraction of converted hydrogen (dash-dotted line).

H. Sensitivity to helium, oxygen, and neon

Time-of-flight measurements were used to separate truly converted, sputtered, and recoiled ions from the conversion surface. For these measurements the ion beam from the MEFISTO source was pulsed by an electrostatic gate prior deceleration to the desired energy and subsequent neutralization. By recording the arrival time at the imaging detector, sputtered, recoiled, and truly converted particle populations could be separated. Measurements were done using neutral hydrogen, neutral helium, neutral oxygen, and neutral neon with the ESA set to bin 4 with 102 eV center energy. The setup allowed us to separate hydrogen, helium, and the sum of carbon and oxygen. The results are summarized in Table IV. Although helium has a metastable negative charge state, the negative ion fraction for helium obtained from the conversion surface is below 5×10^{-5}. Neon does not have a negative charge state, so the signal obtained from incident neutral neon consists entirely of sputtered and recoiled particles. The ionization efficiency for negative oxygen ions fits well to data obtained from earlier experiments [Fig. 17(b)].

TABLE IV. Neutral-to-negative ionization yield for different species.

Incident neutral species	Negative ion fraction	Sputtered and recoiled negative ions
100 eV H	0.023 H^-	$<2\times10^{-3}$ (O^-+C^-)
100 eV He	$<5\times10^{-5}$ He^-	4.6×10^{-3} H^-; 1.6×10^{-3} (O^-+C^-)
100 eV O	0.04 O^-	$<2\times10^{-3}$ H^-
100 eV Ne	0.0 Ne^-	No absolute data available

IV. DISCUSSION

A. Energy resolution

The required energy resolution was the most difficult parameter to achieve during the ion-optical optimization of the IBEX-Lo sensor because it strongly conflicted with transmission and the angular divergence of the trajectories at the exit of the ESA. The measured value of $\Delta E/E \sim 0.98$ for hydrogen includes the energy spread introduced at the ion beam neutralizer[28] and on the prototype conversion surface of each approximately 15% of the incident particle energy. After accounting for these spreads, the energy resolution of the ESA corresponds well with the value predicted in simulations of 0.7, where these energy-spreading processes were not included.

B. Conversion efficiency and geometric factor

The neutral-to-negative ion conversion efficiency of the ta-C DLC surfaces is consistent with data measured on other experiments (Fig. 17). Different batches from conversion surface production showed no significant difference in performance,[26] indicating a well characterized production process suitable for larger quantities required for the flight instrument of IBEX-Lo.

The energy dependence of the geometric factor at low energies is due to the energy dependence of the conversion efficiency. The limited postacceleration voltage relative to the incident particle energy causes a distinct rollover in the geometric factor around 70 eV for 2 kV postacceleration (Fig. 18). At the nominal postacceleration of 20 kV the rollover in the geometric factor will move up to 300 eV neutral particle energy. As neutral particle fluxes are expected to decrease with increasing energy[14,15] it is advantageous to move the rollover to as high energies as possible. Furthermore, a high postacceleration voltage will improve the detection efficiency of the carbon foil based TOF detector that will be used in a flight version of the instrument in place of the present detectors. This is important for the detection of neutral oxygen as the transparency of carbon foils drops very fast below energies of 1 keV/nucleon.

C. Suppression of scattered particles

Particles scattered inside the ion-optical system onto surfaces other than the conversion surface are an important background source. Considerable effort was needed to effectively suppress scattering off inner surfaces. The main complication is the large gap between the ESA electrodes needed to collect a wide angular range of particles reflected from the conversion surface. This large gap allows particles and light scattered at these electrodes to propagate deep into the instrument without hitting another surface. Acceptable suppression was achieved by blackening all exposed inner surfaces along with fins in the outer ESA electrode and serrations in the preaccelerator electrodes. The drawback of this solution is the substantially increased complexity when assembling the sensor due to the mechanical sensitivity of the blackened surfaces.

D. Suppression of secondary electrons

Secondary electrons created by particle impact onto surfaces and photoelectrons both need to be suppressed separately as they cannot be distinguished by the electrostatic ion optics from neutrals converted to negative ions at the conversion surface. Depending on where the electrons are generated, substantial background is generated in energy bins 1 and 2. The suppression of these electrons with permanent magnets placed in the preaccelerator electrodes was very successful. No noticeable effect on the trajectories of negatively ionized hydrogen was observed, and although only one quarter of the circumference of the prototype was equipped with magnets, the field strength in the center axis of symmetry of the instrument was <0.1 mT, a value which does not interfere with the capture of secondary electrons in the TOF unit to be installed in the instrument. The magnets resulted in a significant background reduction at low energies. Above 80 eV incident particle energy the total signal at the detector increases even with magnets because particles sputtered or recoiling from the conversion surface become important. The sputtered and recoiling fraction will be subtracted in a flight instrument by making use of data obtained from higher energy bins.

E. Sensitivity to helium, oxygen, and neon

In space, when looking with the sensor into the interstellar oxygen beam, neutral interstellar helium will also hit the conversion surface. It is very likely that no metastable negative charge state of helium is excited at the conversion surface (Table IV) and the instrument will not directly see helium. Our value of $<5\times10^{-5}$ negative helium ion fraction is limited by counting statistics. Nevertheless the signature of helium will be visible due to sputtering of conversion surface atoms by neutral helium, similar to the detection scheme used by the Ulysses GAS sensor.[11] The sensitivity of the prototype to neutral oxygen is, depending on the energy range, roughly ten times larger than the sensitivity to neutral hydrogen. This is mainly due to the steep increase of the ionization efficiency above 150 eV. The energy resolution of the instrument for neutral oxygen is lower than for neutral hydrogen due to better mass match between the incident neutral atom and the conversion surface atoms (carbon). Energy losses during scattering from the surface are well modeled by elastic collisions for the given collision geometry. However, the lower energy resolution has no impact on the observation of the interstellar oxygen beam as this beam is almost monoenergetic compared to the energy resolution of the electrostatic analyzer in the instrument.

F. Flight model design

Several modifications were done for the design of the flight version of the IBEX-Lo instrument based on the results obtained from the prototype. The modifications include a reduction in the number of electrodes used in the ion-optical system, the change from a circular exit hole of the ESA to a ring-shaped one, the flipping of the conversion surface cone to reflect ionized particles away from the instrument axis of symmetry and thus obtain a longer path in the ESA for better

energy resolution and better suppression of light and scattered particles, and the inclusion of mechanical elements needed for the stiffness of the structure. Also, in a flight version the detector section is replaced by a time-of-flight section that will provide mass resolution for the instrument. About half a year of additional ion-optical simulations and optimizations were needed to reach a flight qualifying ion-optical design.

V. CONCLUSIONS

We have successfully developed, built, and tested the prototype for the IBEX-Lo sensor. New computer-based optimization methods for the ion-optical design along with streamlined design and manufacturing allowed us to do an end-to-end test of the sensor within the short available time frame allowed for by the NASA SMEX-class satellite programme. All necessary measurements were done and valuable expertise could be gained for the development of the flight version of the sensor to be ready for launch into very high Earth orbit onboard the Interstellar Boundary Explorer spacecraft, IBEX, in summer 2008.

ACKNOWLEDGMENTS

The authors thank Joseph Fischer, Harry Mischler, and Jürg Jost for their support when performing the experiments, Adrian Etter for the operation of the CASYMS test facility, and Reto Karrer for help with measurements of the collimator and for the operation of the MEFISTO test facility. This work is supported by the Swiss National Science Foundation and PRODEX.

[1] P. C. Frisch, Space Sci. Rev. **72**, 499 (1995).
[2] E. C. Stone, A. C. Cummings, F. B. McDonald, B. Heikkila, N. Lal, and W. R. Webber, Science **309**, 2017 (2005).
[3] V. B. Baranov and Y. G. Malama, J. Geophys. Res. **98**, 15157 (1993).
[4] H. J. Fahr, T. Kausch, and H. Scherer, Astron. Astrophys. **357**, 268 (2000).
[5] G. P. Zank and H.-R. Müller, J. Geophys. Res. **108**, 1240 (2003).
[6] E. Mobius, D. Hovestadt, B. Klecker, M. Scholer, G. Gloeckler, and F. M. Ipavich, Nature (London) **318**, 6045 (1985).
[7] G. Gloeckler, A. B. Galvin, F. M. Ipavich, J. Geiss, H. Balsiger, R. von Steiger, L. A. Fisk, K. W. Ogilvie, and B. Wilken, Science **261**, 70 (1993).
[8] H.-J. Fahr, Adv. Space Res. **34**, 3 (2004).
[9] G. P. Zank and H. L. Pauls, Space Sci. Rev. **78**, 95 (1996).
[10] G. E. Thomas, Annu. Rev. Earth Planet Sci. **6**, 173 (1978).
[11] M. Witte, H. Rosenbauer, E. Keppler, H. Fahr, P. Hemmerich, H. Lauche, A. Loidl, and R. Zwick, Astron. Astrophys. **92**, 333 (1992).
[12] M. Witte, M. Banaszkiewicz, and H. Rosenbauer, Space Sci. Rev. **78**, 289 (1996).
[13] M. Witte, M. Banaszkiewicz, H. Rosenbauer, and D. McMullin, Adv. Space Res. **34**, 61 (2004).
[14] M. Gruntman, E. C. Roelof, D. G. Mitchell, H. J. Fahr, H. O. Funsten, and D. J. McComas, J. Geophys. Res. **106**, 15767 (2001).
[15] P. Wurz, A. Galli, S. Barabash, and A. Grigoriev, AIP Conf. Proc. **858**, 269 (2006).
[16] D. J. McComas, F. Allegrini, P. Bochsler, M. Bzowski, M. Collier, H. Fahr, H. Fichtner, P. Frisch, H. Funsten, S. Fuselier, G. Gloeckler, M. Gruntmann, V. Izomdenov, P. Knappenberger, M. Lee, S. Livi, D. Mitchell, E. Moebius, T. Moore, D. Reisenfeld, E. Roelof, N. Schwadron, M. Wieser, M. Witte, P. Wurz, and G. P. Zank, AIP Conf. Proc. **719**, 162 (2004).
[17] E. Möbius, S. Fuselier, M. Granoff, E. Hertzberg, B. King, H. Kucharek, S. Livi, S. Longworth, N. Paschalidis, L. Saul, J. Scheer, C. Schlemm, M. Wieser, and P. Wurz, Proceedings of the 30th International Cosmic Ray Conference, Merida, Mexico (unpublished).
[18] H. Réme J. M. Bosqued, J. A. Sauvaud, A. Cros, J. Dandouras, C. Aoustin, C. Martz, J. L. Male, J. Rouzaud, E. Moebius, C. Krocker, M. Granoff, L. M. Kistler, D. Hovestadt, B. Kleckler, G. Paschmann, M. Ertl, E. Knneth, C. W. Carlson, D. W. Curtis, R. P. Lin, J. P. NcFadden, J. Croyle, V. Formisano, M. Di-Lellis, R. Bruno, M. B. Bavassano-Cattaneo, B. Baldetti, G. Chionchio, E. G. Shelley, A. G. Ghielmetti, W. Lennartsson, A. Korth, H. Rosenbauer, I. Szemerey, R. Lundin, S. Olsen, G. K. Parks, M. McCarthy, and H. Balsiger, Space Sci. Rev. **79**, 303 (1997).
[19] P. Wurz, M. R. Aellig, P. Bochsler, A. G. Ghielmetti, E. G. Shelley, S. Fuselier, F. Herrero, M. F. Smith, and T. Stephen, Opt. Eng. (Bellingham) **34**, 2365 (1995).
[20] T. E. Moore, D. J. Chornay, M. R. Collier, F. A. Herrero, J. Johnson, M. A. Johnson, J. W. Keller, J. F. Laudadio, J. F. Lobell, K. W. Ogilvie, P. Rozmarynowski, S. A. Fuselier, A. G. Ghielmetti, E. Hertzberg, D. C. Hamilton, R. Lundgren, P. Wilson, P. Walpole, T. M. Stephen, B. L. Peko, B. van Zyl, P. Wurz, J. M. Quinn, and G. R. Wilson, Space Sci. Rev. **91**, 155 (2000).
[21] P. Wurz, *The Outer Heliosphere: Beyond the Planets*, (Copernicus Gesellschaft e.V., Katlenburg-Lindau, 2000), p. 251.
[22] P. Wurz, J. Scheer, and M. Wieser, e-J. Surf. Sci. Nanotechnol. **4**, 394 (2006).
[23] H. Moestue, Rev. Sci. Instrum. **44**, 1709 (1973).
[24] A. G. Ghielmetti and E. G. Shelley, Nucl. Instrum. Methods Phys. Res. A **298**, 181 (1990).
[25] M. Wieser, Ph.D. thesis, University of Bern, 2005.
[26] J. A. Scheer, M. Wieser, P. Wurz, P. Bochsler, E. Hertzberg, S. A. Fuselier, F. A. Koeck, R. J. Nemanich, and M. Schleberger, Adv. Space Res. **38**, 664 (2006).
[27] E. Moebius, L. M. Kistler, M. A. Popecki, K. N. Crocker, M. Granoff, S. Turco, A. Anderson, P. Demain, J. Distelbrink, I. Dors, P. Dunphy, S. Ellis, J. Gaidos, J. Googins, R. Hayes, G. Humphrey, H. Kästle, J. Lavasseur, E. J. Lund, R. Miller, E. Sartori, M. Shappirio, S. Taylor, P. Vachon, M. Vosbury, V. Ye, D. Hovestadt, B. Klecker, H. Arbinger, E. Künneth, E. Pfeffermann, E. Seidenschwang, F. Gliem, K.-U. Reiche, K. Stöckner, W. Wiewesiek, A. Harasim, J. Schimpfle, S. Battell, J. Cravens, and G. Murphy, Space Sci. Rev. **86**, 449 (1998).
[28] M. Wieser and P. Wurz, Meas. Sci. Technol. **16**, 2511 (2005).
[29] M. Wieser, P. Wurz, R. J. Nemanich, and S. A. Fuselier, J. Appl. Phys. **98**, 03906-1–034906-4 (2005).
[30] Collini Flühmann, Galv. Anstalt, Ringstrasse 9, Postfach 630, 8600 Dübendorf, Switzerland.
[31] T. Zurbuchen, P. Bochsler, and F. Scholze, Opt. Eng. (Bellingham) **34**, 1303 (1995).
[32] A. G. Ghielmetti, H. Balsiger, R. Bänninger, P. Eberhardt, J. Geiss, and D. T. Young, Rev. Sci. Instrum. **54**, 425 (1983).
[33] A. Marti, R. Schletti, P. Wurz, and P. Bochsler, Rev. Sci. Instrum. **72**, 1354 (2001).
[34] Quantar Technology Inc., CA, USA, model 3395A-SE/2401B.
[35] M. Wieser, P. Wurz, P. Bochsler, E. Moebius, J. Quinn, S. A. Fuselier, A. Ghielmetti, J. N. DeFazio, T. M. Stephen, and R. J. Nemanich, Meas. Sci. Technol. **16**, 1667 (2005).